A Novel Flux-weakening Control Method with Quadrature Voltage Constrain for Electrolytic Capacitorless PMSM Drives

Junya Huo, Dawei Ding, *Member, IEEE*, Zekun Ren, Gaolin Wang, *Senior Member, IEEE*, Nannan Zhao, *Member, IEEE*, Lianghong Zhu and Dianguo Xu, *Fellow, IEEE*

***Abstract*—In electrolytic capacitorless permanent magnet synchronous motor (PMSM) drives, the DC-link voltage will fluctuate in a wide range due to the use of slim film capacitor. When the flux-weakening current is lower than $-\psi_f/L_d$ during the high speed operation, the flux-weakening control loop will transform to a positive feedback mode, which means the reduction of flux-weakening current will lead to the acceleration of the voltage saturation, thus the whole system will be unstable. In order to solve this issue, this paper proposes a novel flux-weakening method for electrolytic capacitorless motor drives to maintain a negative feedback characteristic of the control loop during high speed operation. Based on the analysis of the instability mechanism in flux-weakening region, a quadrature voltage constrain mechanism is constructed to stabilize the system. Meanwhile, the parameters of the controller are theoretically designed for easier industrial application. The proposed algorithm is implemented on a 1.5kW electrolytic capacitorless PMSM drive to verify the effectiveness of the flux-weakening performance.**

***Index Terms*—Permanent magnet synchronous motor (PMSM), Electrolytic capacitorless drive, Flux-weakening control, Voltage constrain, Stable operation.**

I. INTRODUCTION

PERMANENT magnet synchronous motors (PMSMs) have been widely used in white goods and other industrial applications due to the merits of higher power density, lower cost and higher efficiency [1]-[4]. In traditional drives, the large-volume electrolytic capacitors are commonly used for energy storage and buffering [5]-[6]. However, the existence of electrolytic capacitors will not only increase the volume but also reduce the reliability of the drives. Because of the short life time, the electrolytic capacitor critically affects the reliability of the drive circuit, about 60% of the drive circuit failure are due to the DC-link electrolytic capacitor [7]-[8]. Recently, many researches have been carried out to use slim film capacitors in motor drives which are the so-called electrolytic capacitorless motor drives. Firstly, the largely reduced DC capacitance will increase the power factor of the grid side, and the Power Factor Correction (PFC) can be removed, which leads to remarkable cost and volume reduction [9]-[11]. Then, the film capacitors have stronger tolerance of ripple voltage, which are more suitable for power electronics system and can prolong the service time of drives [12]-[13].

However, the slim DC-link capacitor cannot be regarded as an energy buffer anymore, which will aggravate the energy coupling between the grid side and the motor side. Consequently, some new challenges will happen such as the LC resonance [14]-[17], high power quality control [18]-[19], beat phenomenon [20]-[25], and more difficult flux-weakening control in high-speed operation [26]-[28].

The inverter controlled PMSM can be regarded as constant power loads (CPLs), which will aggravate the system LC resonance and even lead to instability in a weak grid. Some strategies have been proposed to solve the instability problem of the electrolytic capacitorless motor drives, and they can be classified into two categories. One solution is algorithm based, which means changing the frequency characteristics of the drive by manipulating the motor power [14]-[16]. The other solution is hardware based, which means modifying the power circuit by adding additional switching devices [17], this kind of methods is less attractive because of increased cost. In [14], an active damping control method was proposed based on DC-link voltage closed loop control, the system could be stable due to the increase of the system damping characteristic. In [16], the stability control was analyzed based on speed sensorless control, the stability scheme was designed by taking the motor side characteristics into consideration.

The power factor of the grid side should be higher than 0.95 in the application of white goods. So, it is important to develop high power factor control strategy for the application of electrolytic capacitorless motor drives. Modifying the grid power can realize the improvement of the power factor. Considering that the grid voltage will not change with load power, modifying the amplitude and phase of the grid current

Manuscript received October 10, 2021; revised February 15, 2022; accepted April 26, 2022. date of publication September 25, 2022; date of current version September 18, 2022

This work was supported in part by the Research Fund for the National Natural Science Foundation of China under Grant 52125701, 52007039, 51877054 and in part by the Key areas R&D Program of Guangdong Province China under Grant 2021B0101310001.*(Corresponding Author: Gaolin Wang)*

Junya Huo and Lianghong Zhu are with the the School of Electrical Engineering and Automation, Harbin Institute of Technology, Harbin 150001, China, and also with the Guangdong Midea Air-Conditioning Equipment Co., Ltd., Foshan 528311, China (e-mail: 17b906042@stu.hit.edu.cn; zhulh@midea.com.cn).

Dawei Ding, Zekun Ren, Gaolin Wang, Nannan Zhao, and Dianguo Xu are with the School of Electrical Engineering and Automation, Harbin Institute of Technology, Harbin 150001, China (e-mail: dingdawei@hit.edu.cn; neaurenzekun@163.com; WGL818@hit.edu.cn; xudiang@hit.edu.cn).

Digital Object Identifier 10.30941/CESTEMS.2022.00038

can realize the improvement of the grid power quality. Based on this concept, many kinds of methods have been proposed. In [18], the optimal q-axis current was calculated based on online method to compensate the grid current. In [19], the grid power was controlled by motor torque, which simplified the design of parameters.

Due to the fluctuated DC-link voltage, the traditional flux-weakening control methods cannot obtain satisfactory performance in electrolytic capacitorless drives. In [26], a unique method named hexagon voltage manipulating (HVMC) was proposed, which accomplished the maximum voltage utilization by eliminating the current control loop. In order to eliminate the torque ripple, the voltage reference was limited to the linear modulation range, that is, the minimum DC-link voltage was chosen as the voltage limit [27]. An effective strategy based on average voltage constrain is proposed in [10] for electrolytic capacitorless motor drives. However, the range of the d-axis current is just limited in $[-\psi_f/L_d,0]$. A practical flux-weakening method was proposed in [28]. The d-axis flux-weakening current was produced by the q-axis voltage difference between the reference and the real values through a low-pass filter. The output of the stator voltage can be extended beyond the hexagon of the minimum DC-link voltage stably by using this flux-weakening method.

The aforementioned methods have rendered the flux-weakening control in the electrolytic capacitorless motor drives a great improvement in voltage utilization and torque ripple. However, the instability issue in deep flux-weakening region is seldom reported. The valley of the DC-link voltage is only dozens of volts with 220V (50Hz) AC power supply. Thus, the motor is always operating in the flux-weakening region, and will enter into the deep flux-weakening region when the speed gets higher. Under this situation, conventional voltage closed loop flux-weakening methods will enter into positive feedback mode, which will cause system instability.

In this paper, a novel flux-weakening method is investigated. With the proposed method, the flux-weakening control loop can always work in negative feedback mode, and the system can be stable in deep flux-weakening region. The instability issue in deep flux-weakening control is discussed based on the small signal model of the control loop when using the conventional voltage feedback method. Based on the analysis, a flux-weakening method with quadrature voltage constrain is proposed to solve the instability problem in the deep flux-weakening region. The parameters of the flux-weakening controller are theoretically designed to balance the voltage utilization and stability.

This paper proceeds as follows: the description of the unstable problem in deep flux-weakening region when using the conventional method is displayed in Section II. Section III introduces the proposed flux-weakening method with voltage constrain. Experimental results to verify the proposed flux-weakening method are in Section IV.

II. Analysis of Flux Weakening Method in Reduced DC-Link Capacitance PMSM Drives

A. Discussion of Voltage Closed Loop Flux-Weakening Method

The conventional voltage closed loop control method is shown in Fig. 1. The direct axis current is generated by the voltage control loop to increase the motor speed when the motor voltage is saturated.

Assuming that the grid voltage is an ideal sine wave

$$u_g = U_m \sin(\theta_g) \tag{1}$$

where U_m and θ_g are the amplitude and phase of the source voltage, respectively.

In electrolytic capacitorless motor drives, the DC-link capacitance is only 1/50 of the original value, which leads to great DC-link voltage fluctuation at twice the frequency of the grid voltage. For the air conditioning drive with reduced DC-link capacitance, the DC-link voltage is not allowed to fall to zero, and it needs to be maintained above a certain value to realize the reliable operation of the motor.

According to Fig. 2, the command of the DC-link voltage can be set as

$$u_{dc}^* = \begin{cases} U_m \sin\theta_{gm} & \theta_{gm} \in [\theta_d, \pi-\theta_d] \\ u_{dcmin} & \theta_{gm} \in [0,\theta_d) \cup (\pi-\theta_d, \pi] \end{cases} \tag{2}$$

where θ_d is the zero-current dead zone of the source, u_{dcmin} is the minimum of the DC-link voltage, and u_{dcmax} is the maximum of

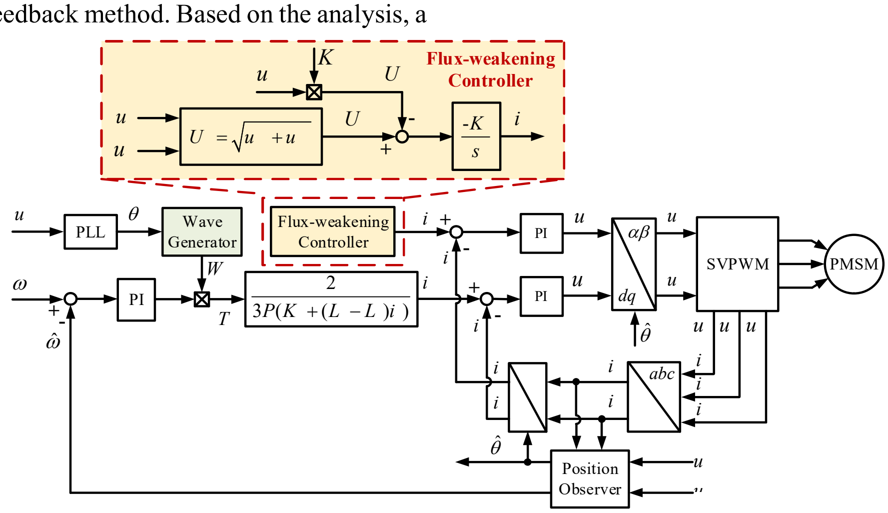

Fig. 1. Block diagram of voltage closed loop flux-weakening control method.

the DC-link voltage which is equal to U_m. $u_{dcmin}=U_m\sin\theta_d$, $u_{dcmax}=U_m$, and $\theta_{gm}=\mathrm{mod}(\theta_g, \pi)$. In order to ensure the reliable operation of motor, it is necessary to keep the DC-link voltage above u_{dcmin}.

The voltage equation of PMSM can be presented as

$$\begin{cases} u_d = i_d R_s + L_d \dfrac{di_d}{dt} - \omega_e i_q L_q \\ u_q = i_q R_s + L_q \dfrac{di_q}{dt} + \omega_e i_d L_d + \psi_f \omega_e \end{cases} \quad (3)$$

where u_d and u_q are the d- axis and q-axis voltage, i_d and i_q are the d-axis and q-axis current, L_d and L_q are the d-axis and q-axis inductance, ω_e is the motor speed, R_s is the stator resistance, and ψ_f is the flux linkage.

The q-axis current command can be presented as

$$\begin{cases} T_e^* = W_f * (k_p + \dfrac{k_i}{s})(\omega_e^* - \omega_e) \\ i_q^* = \dfrac{2T_e^*}{3p(\psi_f + (L_d - L_q) i_d)} \end{cases} \quad (4)$$

where T_e^*, i_q^* and ω_e^* are the commands of the torque, the q-axis current, and the speed, respectively. PI represents proportional and integral regulator. W_f is the wave generator.

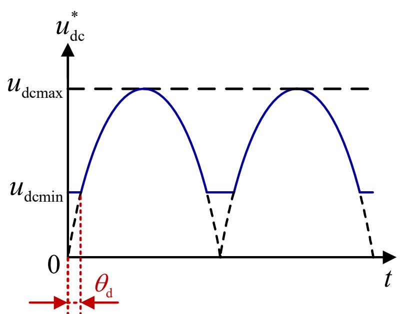

Fig. 2. Schematic diagram of the DC-link voltage of IPMSM drive with reduced DC-link capacitance.

For electrolytic capacitorless motor drive, the input current and voltage can be synchronous sine waves ideally. Ignoring the capacitor power, the input and output power of the inverter are the same

$$\begin{cases} P_g = U_m I_m \sin^2(\theta_{gm}) \\ P_{out} = T_e^* \omega_e \\ P_g = P_{out} \end{cases} . \quad (5)$$

According to (5), the waveform of the input power is the square of sine. Therefore, the waveform generator W_f can be set as

$$W_f = \sin^2(\theta_{gm}) . \quad (6)$$

According to (4) and (6), the q-axis current command can be expressed as

$$\begin{cases} i_q^* = I_{q0} \sin^2 \theta_{gm} \\ I_{q0} = \dfrac{2 * (k_p + \dfrac{k_i}{s})(\omega^* - \omega)}{3p(\psi_f + (L_d - L_q) i_d)} \end{cases} . \quad (7)$$

In order to avoid the instability of the system when the DC-link voltage is lower than the minimum limit value u_{dcmin}. The q-axis current command is set to 0 in the zero-current dead zone of the source θ_d.

$$i_q^* = \begin{cases} I_{q0} \sin^2 \theta_{gm} & \theta_{gm} \in [\theta_d, \pi - \theta_d] \\ 0 & \theta_{gm} \in [0, \theta_d) \cup (\pi - \theta_d, \pi] \end{cases} . \quad (8)$$

According to (3) and (7), the stator voltage can be re-expressed as

$$\begin{cases} u_d = i_d R_s + L_d \dfrac{di_d}{dt} - \omega_e I_{q0} L_q \sin^2 \theta_g \\ u_q = I_{q0} R_s \sin^2 \theta_g + I_{q0} L_q \sin(2\theta_g) + \omega_e L_d i_d + \psi_f \omega_e \end{cases} . \quad (9)$$

When the motor is in steady-state operation, ignoring the voltage drop of stator resistance and inductance, (9) can be simplified as

$$\begin{cases} u_d = -\omega_e I_{q0} L_q \sin^2 \theta_g \\ u_q = \omega_e L_d i_d + \psi_f \omega_e \end{cases} . \quad (10)$$

Considering the output capacity of the inverter, the constraint equations of stator current I_s and stator voltage U_S can be expressed as

$$\begin{cases} I_s = \sqrt{i_d^2 + i_q^2} \le I_{max} \\ U_S = \sqrt{u_d^2 + u_q^2} \le U_{max} \end{cases} \quad (11)$$

where I_{max} is the maximum current, U_{max} is the maximum voltage that can be output by the inverter. Considering the linear modulation of the voltage, U_{max} is $u_{dc}/\sqrt{3}$.

Fig.3 shows the current and voltage constrain of the motor drive with reduced DC-link capacitance. The current constraint is a circle with I_{sm} as the radius. In the electrolytic capacitorless motor drive system, the voltage limit ellipse changes with the fluctuated DC-link voltage between ellipse u_{dcmax} and u_{dcmin} at the same speed as shown in Fig. 3. Assuming that the motor speed is ω_1, when the DC-link voltage reaches the maximum value, the voltage limit circle is the blue biggest ellipse. When the DC-link voltage reaches the minimum value, the voltage limit circle is the blue smallest ellipse.

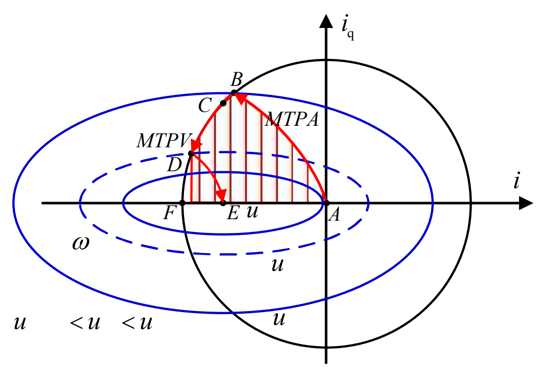

Fig. 3. Current and voltage constrain of motor drive with reduced DC-link capacitance.

When the speed increases, $\psi_f\omega_e$ will increase accordingly, which leads to insufficient DC-link voltage margin. In order to deal with the problem, the q-axis current command is designed to be dynamically adjusted with the source voltage cycle, as shown in (7). According to (10), the d-axis voltage can be dynamically adjusted with the grid voltage cycle to ensure that the d-axis voltage meets the requirement of the voltage limit circle as shown in Fig. 3 in real time. In order to make the q-axis voltage meet the voltage limit circle shown in Fig. 3, the negative d-axis current i_d should be applied through flux-weakening control to reduce u_q.

The voltage feedback flux-weakening control can be expressed as

$$\begin{cases} U_S^* = \sqrt{u_d^{*2} + u_q^{*2}} \\ i_d^* = \dfrac{-K_i}{s}(U_S^* - U_{max}) \end{cases} . \tag{12}$$

B. Instability Issue When Applying Flux-Weakening Control Strategy

The conventional flux-weakening control strategy has the instability problem when the voltage is saturated. According to the flux-weakening control strategy shown in (12) and the voltage equation model shown in (3), the small signal model of the conventional voltage feedback flux-weakening control method can be obtained, as shown in Fig. 4.

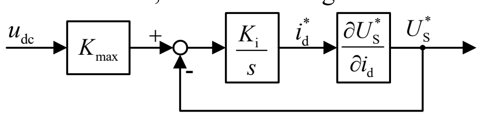

Fig. 4. Small signal model of conventional voltage feedback flux-weakening control method.

In Fig. 4, $\partial U_S^* / \partial i_d$ represents the d-axis current change on U_S^*. According to (3) and (12),

$$\frac{\partial U_S^*}{\partial i_d} = \frac{\partial U_S^*}{\partial u_d}\frac{\partial u_d}{\partial i_d} + \frac{\partial U_S^*}{\partial u_q}\frac{\partial u_q}{\partial i_d} = \frac{u_d R_s + u_q \omega_e L_d}{\sqrt{u_d^2 + u_q^2}} . \tag{13}$$

According to the closed loop model shown in Fig. 4, when $\partial U_S^* / \partial i_d > 0$, U_s^* is the increasing function of i_d, and the closed-loop system is negative feedback, which is stable. When $\partial U_S^* / \partial i_d < 0$, U_s^* is the decreasing function of i_d, and the closed loop system is positive feedback, which is unstable.

In combination with (13), the conditions for stability can be expressed as

$$u_d R_s + u_q \omega_e L_d > 0 . \tag{14}$$

When the motor is running at high speed, (14) can be simplified as $u_q>0$. Once (14) cannot be satisfied, which means $u_q \leq 0$, the system will be unstable.

According to (10), once $i_d<-\psi_f/L_d$, u_q will be less than 0, and the traditional flux-weakening control system will be unstable.

III. Proposed Flux-Weakening Control Strategy for Electrolytic Capacitorless Drive System

A. Structure of the Flux-Weakening Method With Quadrature Voltage Constrain

In order to solve the instability problem of conventional flux-weakening control, a novel flux-weakening control strategy based on the feedback of quadrature axis voltage is proposed, the diagram is shown in Fig. 5. Different from the conventional voltage feedback flux-weakening method, the quadrature voltage information is introduced to the voltage loop to increase the stability of the flux-weakening control.

The current command of flux-weakening control based on the feedback of q-axis voltage can be presented as

$$\begin{cases} i_d^* = \dfrac{-K}{\tau s+1}(u_q^* - u_{qmax}) \\ u_{qmax} = u_q^* \dfrac{\min(U_{max}, U_S^*)}{U_S^*} \end{cases} \tag{15}$$

where τ is the time constant of the low-pass filter, and K is the proportional gain of flux-weakening controller.

Eq. (15) can be presented as

$$i_d^* = \begin{cases} \dfrac{-K}{\tau s+1}(u_q^* - u_{qmax}^*) & U_S^* > U_{max} \\ 0 & U_S^* \leq U_{max} \end{cases} . \tag{16}$$

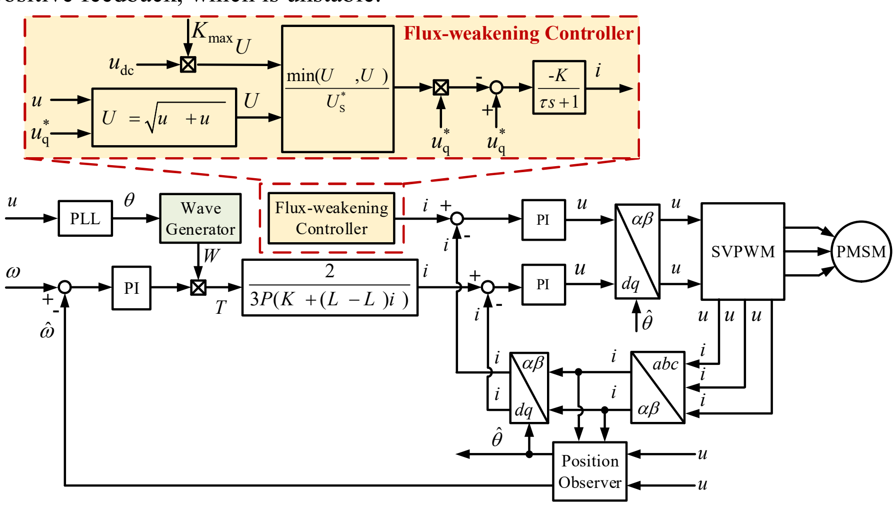

Fig. 5. Block diagram of novel flux-weakening control strategy with quadrature voltage constrain.

$\partial u_q^* / \partial i_d$ represents the influence of d-axis current variation on u_q^*, and the small signal model of the closed-loop system of the proposed flux-weakening control system can be shown in Fig. 6.

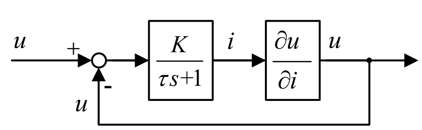

Fig. 6. Small signal model of the proposed flux-weakening control method.

According to (3),

$$\frac{\partial u_{\mathrm{q}}^{*}}{\partial i_{\mathrm{d}}}=\omega_{\mathrm{e}}L_{\mathrm{d}}\,. \tag{17}$$

It can be seen from (17) that $\partial u_{\mathrm{q}}^{*}/\partial i_{\mathrm{d}}>0$, the flux-weakening closed-loop system is negative feedback, which is stable.

B. Analysis of Parameter Influence on Flux-Weakening Control Strategy

The DC-link voltage fluctuation period is twice of the source voltage. In order to obtain a stable flux-weakening current, the cutoff frequency of the low-pass filter is preferably set to 1/10 of DC-link frequency.

The q-axis voltage command can be presented as

$$u_{\mathrm{q}}^{*}=\psi_{\mathrm{f}}\omega_{\mathrm{e}}+i_{\mathrm{d}}^{*}L_{\mathrm{d}}\omega_{\mathrm{e}}+PI(i_{\mathrm{q}}^{*}-i_{\mathrm{q}})\,. \tag{18}$$

Combined with (15) and (18),

$$u_{\mathrm{q}}^{*}=\psi_{\mathrm{f}}\omega_{\mathrm{e}}+\frac{KL_{\mathrm{d}}\omega_{\mathrm{e}}}{\tau s+1}(u_{\mathrm{qmax}}-u_{\mathrm{q}}^{*})+PI(i_{\mathrm{q}}^{*}-i_{\mathrm{q}})\,. \tag{19}$$

Fig. 7 is the schematic diagram of the q-axis voltage command and the q-axis saturation voltage. It can be seen from Fig. 7 that $u_{\mathrm{qmax}}-u_{\mathrm{q}}^{*}$ satisfies

$$u_{\mathrm{qmax}}-u_{\mathrm{q}}^{*}=u_{\mathrm{q}}^{*}\frac{U_{\max}-U_{\mathrm{S}}^{*}}{U_{\mathrm{S}}^{*}}\,. \tag{20}$$

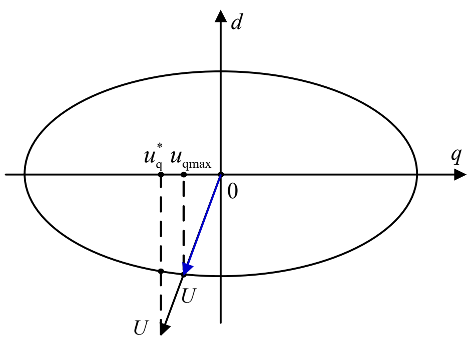

Fig. 7. Schematic diagram of q-axis voltage command and q-axis saturation voltage.

According to (20) and ignoring the change of speed, (19) can be simplified as

$$\begin{cases}\tau\dot{u}_{\mathrm{q}}^{*}+u_{\mathrm{q}}^{*}=\dfrac{U_{\max}-U_{\mathrm{S}}^{*}}{U_{\mathrm{S}}^{*}}KL_{\mathrm{d}}\omega_{\mathrm{e}}u_{\mathrm{q}}^{*}+\Delta\\[2ex]\Delta=PI(i_{\mathrm{q}}^{*}-i_{\mathrm{q}})+\psi_{\mathrm{f}}\omega_{\mathrm{e}}+\dfrac{dPI(i_{\mathrm{q}}^{*}-i_{\mathrm{q}})}{dt}\end{cases}. \tag{21}$$

In (21), Δ can be regarded as an external disturbance, assuming that the error of q-axis current control is zero and its mean value is $\psi_{\mathrm{f}}\omega_{\mathrm{e}}$, thus (21) can be simplified as

$$\tau\dot{u}_{\mathrm{q}}^{*}=(\frac{U_{\max}-U_{\mathrm{S}}^{*}}{U_{\mathrm{S}}^{*}}KL_{\mathrm{d}}\omega_{\mathrm{e}}-1)u_{\mathrm{q}}^{*}+\psi_{\mathrm{f}}\omega_{\mathrm{e}}\,. \tag{22}$$

According to (20) and (21), it can be obtained

$$\tau\dot{u}_{\mathrm{q}}^{*}+(1+KL_{\mathrm{d}}\omega_{\mathrm{e}})u_{\mathrm{q}}^{*}=\psi_{\mathrm{f}}\omega_{\mathrm{e}}+KL_{\mathrm{d}}\omega_{\mathrm{e}}u_{\mathrm{qmax}}\,. \tag{23}$$

The steady-state value of u_{q}^{*} is

$$u_{\mathrm{qss}}=\frac{\psi_{\mathrm{f}}\omega_{\mathrm{e}}+KL_{\mathrm{d}}\omega_{\mathrm{e}}u_{\mathrm{qmax}}}{1+KL_{\mathrm{d}}\omega_{\mathrm{e}}}\,. \tag{24}$$

Considering the range of *K*, which is larger than 10, and the system parameters shown in Table I, the assumption can be made that $KL_{\mathrm{d}}\omega_{\mathrm{e}}>>1$, then

$$u_{\mathrm{qss}}\approx\frac{\psi_{\mathrm{f}}\omega_{\mathrm{e}}+KL_{\mathrm{d}}\omega_{\mathrm{e}}u_{\mathrm{qmax}}}{KL_{\mathrm{d}}\omega_{\mathrm{e}}}=\frac{\psi_{\mathrm{f}}}{KL_{\mathrm{d}}}+u_{\mathrm{qmax}}\,. \tag{25}$$

Fig. 8 shows the relationship between u_{qss}, u_{qmax} and proportional gain *K*. In conclusion, when the error of q-axis current control is zero, the upper bound of voltage u_{q}^{*} is $u_{\mathrm{qmax}}+\psi_{\mathrm{f}}/(K^{*}L_{\mathrm{d}})$, which will be closer to u_{qmax} with the increase of *K*.

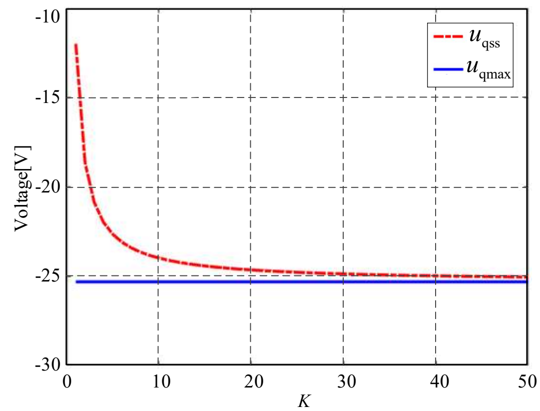

Fig. 8. Schematic diagram of relationship between u_{qss}, u_{qmax}, and proportional gain *K*.

IV. UNITS

In order to verify the effectiveness of the method, experiments are carried out on the 1.5kW motor drive. The test bench is shown in Fig. 9 (a). Fig. 9 (b) shows the electrolytic capacitorless motor drive circuit using Renesas 32-bit MCU rx62t as the control core, and the main frequency is 100 MHz. The compressor motor is driven by IPM, and the carrier frequency of 6 kHz. The DC-link capacitance is 20 μF, and the AC side inductance is 5 mH. The circuit and compressor motor parameters are shown in Table I.

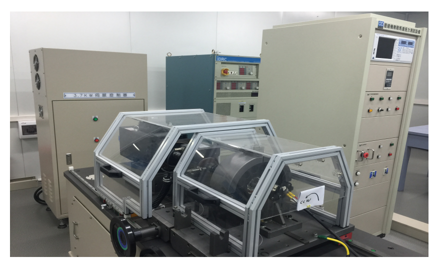

(a)

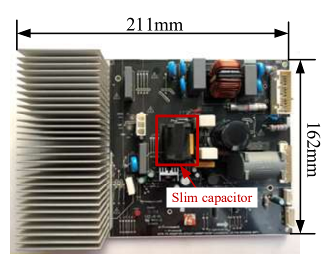

(b)

Fig. 9. Platform of the electrolytic capacitorless motor drive. (a) Test bench. (b) Drive circuit.

TABLE I
SYSTEM PARAMETERS

Parameters	Units	Values
Input voltage	V	220
Voltage frequency	Hz	50
Film capacitor	μF	20
Filter inductance	mH	5
Output power	kW	1.5
Pole pair		3
Motor phase resistance	Ω	1
Flux linkage	Wb	0.108
d-axis inductance	mH	8.1
q-axis inductance	mH	11.6

The comparisons of the conventional method and proposed method in deep flux-weakening region are shown in Fig. 10. When the motor speed reaches 6180 r/min, the direct axis current command reaches -13.5 A, which is less than the characteristic value of the direct axis current of $-\psi_f/L_d$. As can be seen, the direct axis current reduces rapidly, reaches the demagnetization limit value of -19 A within 600 ms, and remains at -19 A, which means the flux-weakening loop is out of control as shown in Fig. 10 (a). In Fig. 10 (b), the motor speed is 6780 r/min and the direct axis current is -16 A. It can be seen that when the direct axis current is less than the characteristic value, the flux weakening control can still operate stably.

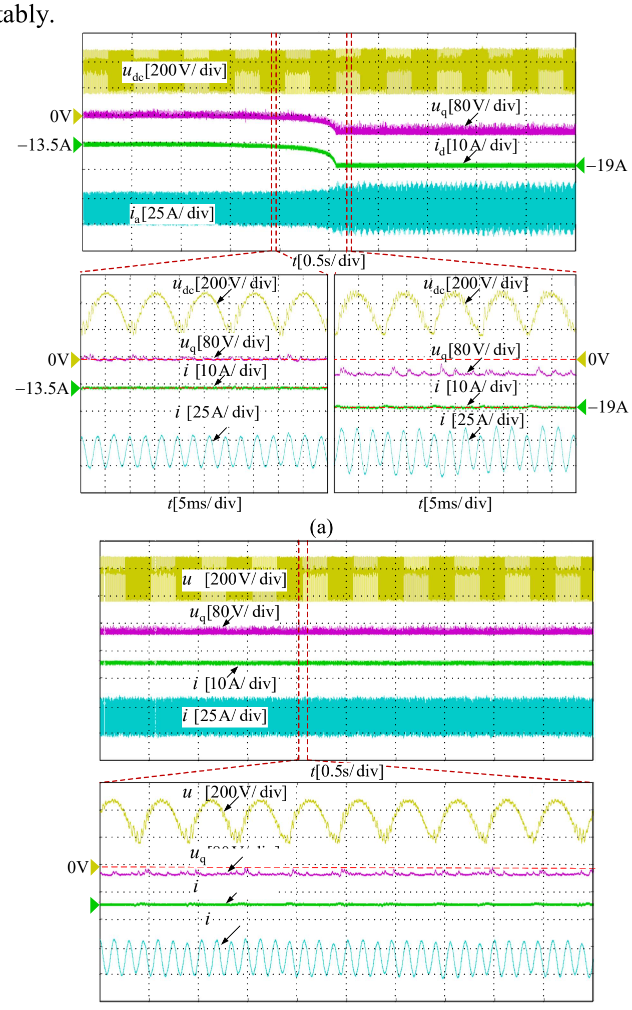

Fig. 10. Experimental results of the comparison in deep flux-weakening region. (a) Conventional method. (b) Proposed method.

Fig. 11 shows the experimental results of the speed dynamic. The motor accelerates from 3000r/min to 6500r/min within 5s, and then the motor decelerates from 6500r/min to 3000r/min within 5s. As can be seen, the motor dynamic process is smooth.

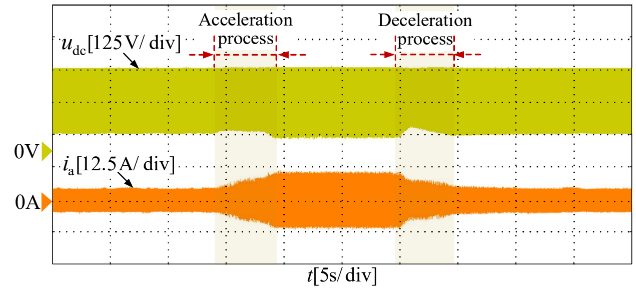

Fig. 11. Experimental results of the speed dynamic process.

Fig. 12 shows the experimental results of the torque dynamic process. At the speed of 5500 r/min, the load torque is decreased from 2 N.m to 0 N.m within 5 s, and then increased to 2 N.m within 8 s. The proposed flux-weakening method can work well in the load dynamic process.

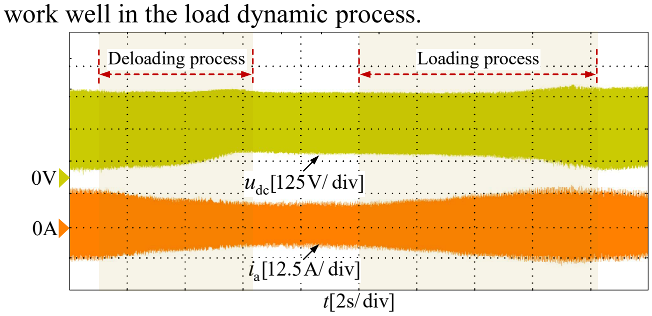

Fig. 12. Experimental results of the torque dynamic process.

The error of q-axis voltage under different K is shown in Fig. 13. The motor speed is 5000 r/min and the torque is 0.5 N.m. The experimental results when K is 10, 20, 30, 40 and 50 are shown in Fig. 13. It can be seen from the figure that the larger the K, the closer the q-axis voltage command to the maximum limit of q-axis voltage. Besides the experimental motor KSN98D22UEZ, some other typical motors of the same rated power are tested. As can be seen, the voltage error can be reduced with the increase of K, and the voltage error is below 0.5 V when K is larger than 35.

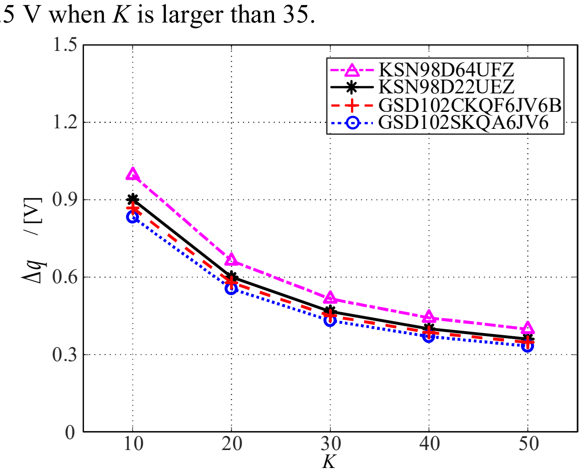

Fig. 13. Error of q-axis voltage under different values of K using the proposed method.

Fig. 14 shows the efficiency experimental results when K is 10, 20, 30, 40 and 50 respectively. As can be seen from the figure, as the increase of K, the system efficiency is getting lower. The driver efficiency of conventional flux-weakening control strategy and proposed flux-weakening control strategy is compared as shown in Fig. 15. The load torque is 0.5 N.m. It can be seen from the figure that the efficiency of conventional flux-weakening and proposed flux-weakening is the same in the speed range of 3000 ~ 6000 r/min.

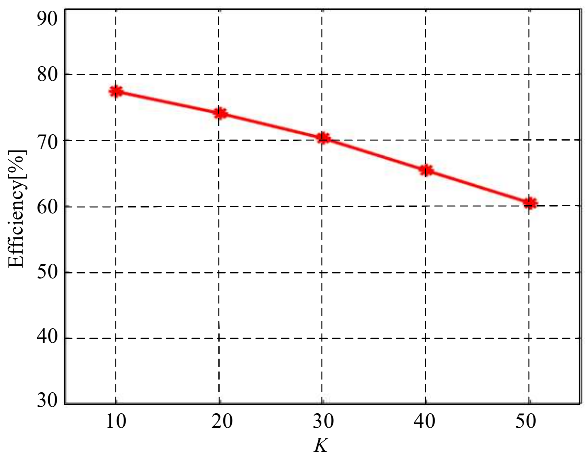

Fig. 14. Efficiency of the proposed flux-weakening method under different K values.

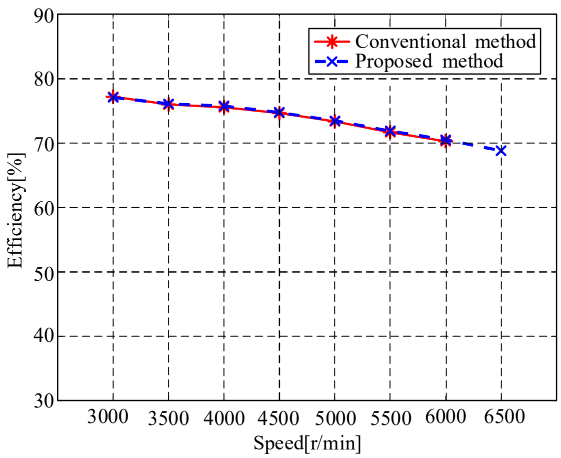

Fig. 15. Comparison of system efficiency.

V. Conclusion

In order to improve the stability of the electrolytic capacitorless motor drives during the deep flux-weakening region caused by the voltage saturation due to the largely fluctuated DC-link voltage, a novel flux-weakening control strategy with quadrature axis voltage constrain has been proposed. The reason of the unstable problem when applying the conventional voltage feedback flux-weakening method is clearly displayed, which may enter into a positive feedback mode when the DC-link voltage is extremely low. Benefited from the introduction of quadrature axis voltage, the stability of the control system is improved during flux-weakening region. Meanwhile, the parameters of the controller are theoretical designed by taking the voltage utilization and stability into consideration. The experimental results show that the novel flux-weakening can work effectively without efficiency sacrifice.

References

[1] C. He, and T. Wu, “Analysis and design of surface permanent magnet synchronous motor and generator,” *CES Trans. Elect. Mach. Syst.*, vol. 3, no. 1, pp. 94-100, Mar. 2019.

[2] L. Li, J. Xiao, Y. Zhao, K. Liu, X. Peng, H. Luan, and K. Li, “Robust position anti-interference control for PMSM servo system with uncertain disturbance,” *CES Trans. Elect. Mach. Syst.*, vol. 4, no. 2, pp. 151-160, Jun. 2020.

[3] X. Ma, and C. Bi, “A technology for online parameter identification of permanent magnet synchronous motor,” *CES Trans. Elect. Mach. Syst.*, vol. 4, no. 3, pp. 237-242, Sept. 2020.

[4] M. Aoyama, and J. Deng, “Visualization and quantitative evaluation of eddy current loss in bar-wound type permanent magnet synchronous motor for mild-hybrid vehicles,” *CES Trans. Elect. Mach. Syst.*, vol. 3, no. 3, pp. 269-278, Sept. 2019.

[5] J. He, L. Huang, D. Wu, C. Zhu, and H. Xin, “Frequency support from PMSG-based wind turbines with reduced DC-link voltage fluctuations,” *CES Trans. Elect. Mach. Syst.*, vol. 2, no. 3, pp. 296-302, Sept. 2018.

[6] H. Wen, W. Xiao, X. Wen and P. Armstrong, “Analysis and Evaluation of DC-Link Capacitors for High-Power-Density Electric Vehicle Drive Systems,” *IEEE Trans. Veh. Technol.*, vol. 61, no. 7, pp. 2950–2964, Sept. 2012.

[7] Y. Son and J. I. Ha, “Direct Power Control of a Three-Phase Inverter for Grid Input Current Shaping of a Single-Phase Diode Rectifier With a Small DC-Link Capacitor,” *IEEE Trans. Power Electron.*, vol.30, no. 7, pp. 3794-3803, Jul. 2015.

[8] Y. Son and J. Ha, “Efficiency Improvement in Motor Drive System with Single Phase Diode Rectifier and Small DC-link Capacitor,” *2014 IEEE Energy Conversion Congress and Exposition (ECCE)*, pp. 3171-3178, 2014.

[9] K. Abe, H. Haga, K. Ohishi, and Y. Yokokura, “Fine Current Harmonics Reduction Method for Electrolytic Capacitor-less and Inductor-less Inverter Based on Motor Torque Control and Fast Voltage Feedforward Control for IPMSM,” *IEEE Trans. Ind. Electron.*, vol. 64, no. 2, pp. 1071-1080, May 2017.

[10] H. S. Jung, S. J. Chee, S. K. Sul, Y. J. Park, H. S. Park, and W. K. Kim, “Control of Three-phase Inverter for AC Motor Drive With Small DC-link Capacitor Fed by Single-phase AC Source,” *IEEE Trans. Ind. Appl.*, vol. 50, no. 2, pp. 1074-1081, 2014.

[11] K. Abe, H. Haga, K. Ohishi, and Y. Yokokura, “Direct DC-link Current Control Considering Voltage Saturation for Realization of Sinusoidal Source Current Waveform Without Passive Components for IPMSM Drives,” *IEEE Trans. Ind. Electron.*, vol. 65, no. 5, pp. 3805-3814, 2018.

[12] Z. Qian, W. Yao, K. Lee, “Dynamic DC-link Over-voltage Mitigation Method in Electrolytic Capacitor-less Adjustable Speed Drive Systems,” *2018 IEEE Energy Conversion Congress and Exposition (ECCE)*, pp. 4628-4632.

[13] D. Ding, G. Zhang, G. Wang, D. Xu, “Dual Anti-overvoltage Control Scheme for Electrolytic Capacitorless IPMSM Drives With Coefficient Autoregulation,” *IEEE Trans. Power Electron.*, vol. 35, no. 3, pp. 2895-2907, 2020.

[14] Y. Araki, K. Ohishi, Y. Yokokura and K. Abe, “MPDCC Based High Efficiency Harmonic Reduction Control for IPMSM Driven by Electrolytic Capacitorless Inverter: *IECON 2018 - 44th Annual Conference of the IEEE Industrial Electronics Society*, 2018, pp. 589-594.

[15] T. Ardriani, L. A. Budiwicaksana, A. I. Putri, J. Furqani, A. Rizqiawan and P. A. Dahono, "Suppressing the Effects of DC Voltage Fluctuation in PWM Inverters by Using Virtual Impedance," *2021 IEEE 12th Energy Conversion Congress & Exposition - Asia (ECCE-Asia)*, 2021, pp. 1922-1927.

[16] Y. Feng, D. Wang and F. Blaabjerg, “Input Admittance Model for the Sensorless Controlled Three-Phase Slim DC-link Drive,” *2018 20th European Conference on Power Electronics and Applications (EPE'18 ECCE Europe)*, pp. P.1-P.9.

[17] H. Shin, Y. Son and J. Ha, “Grid Current Shaping Method with DC-Link Shunt Compensator for Three-Phase Diode Rectifier-Fed Motor Drive System,” *IEEE Trans. Power Electron.*, vol. 32, no. 2, pp. 1279-1288, 2017.

[18] L. Chen, Z. Wei, “Current Tracking Control Strategy for High Power Factor Electrolytic Capacitorless IPMSM Drive System,” *Electric*

Machines and Control, pp. 1-9, 2021.

[19] H. Kai, X. Fenghao, Y. Quan, and L. Hui, "Control Strategy for Permanent Magnet Synchronous Motor Drive System Without Electrolytic Capacitor Based on High Power Factor Control," Electric Machines and Control Application, vol. 46, no. 3, pp. 15-20, 2019.

[20] X. Yue, D. Boroyevich, F. Lee, F. Chen, R. Burgos, F. Zhuo, "Beat frequency oscillation analysis for power electronic converters in DC nanogrid based on crossed frequency output impedance matrix model," *IEEE Trans. Power Electron.*, vol. 33, no. 4, pp. 3052-3064, 2018.

[21] B. Fan, K. Wang, P. Wheeler, C. Gu, Y. Li, "A branch current reallocation based energy balancing strategy for the modular multilevel matrix converter operating around equal frequency," *IEEE Trans. Power Electron.*, vol. 33 no. 2, pp. 1105-1117, 2018.

[22] B. Fan, K. Wang, P. Wheeler, C. Gu, Y. Li, "An optimal full frequency control strategy for the modular multilevel matrix converter based on predictive control," *IEEE Trans. Power Electron.*, vol. 33, no. 8, pp. 6608-6621, 2018.

[23] K. Jiang, C. Zhang, X. Ge, "Low-Frequency Oscillation Analysis of the Train-Grid System Based on an Improved Forbidden-Region Criterion," *IEEE Trans. Ind. Appl.*, vol. 54, no. 5, pp 5064-5073, 2018.

[24] D. Ding, N. Zhao, G Wang, G. Zhang, X. Zhang, N. Mijatovic, and D. Xu, "Suppression of beat phenomenon for electrolytic capacitorless motor drives accounting for sampling delay of DC-link voltage," *IEEE Trans. Ind. Electron.*, doi: 10.1109/TIE.2021.3063984.

[25] N. Zhao, G. Wang, B. Li, R. Zhang, D. Xu, "Beat phenomenon suppression for reduced DC-link capacitance IPMSM drives with fluctuated load torque," *IEEE Trans. Ind. Electron.*, vol. 66, no. 11, pp. 8334-8344, 2019.

[26] J. K. Seok and S. Kim, "Hexagon Voltage Manipulating Control (HVMC) for AC Motor Drives Operating at Voltage Limit" *IEEE Trans. Ind. Appl.*, vol. 51, no. 5, pp. 3829-3837, 2015.

[27] M. Hinkkanen and J. Luomi, "Induction Motor Drives Equipped With Diode Rectifier and Small DC-Link Capacitance," *IEEE Trans. Ind. Electron.*, vol. 55, no. 1, pp. 312-320, 2008.

[28] A. Yoo, S. K. Sul, H. Kim and K. S. Kim, "Flux-Weakening Strategy of an Induction Machine Driven by an Electrolytic-Capacitor-Less Inverter" *IEEE Trans. Ind. Appl.*, vol. 47, no. 3, pp. 1328-1336, 2011.

Junya Huo received the B.S. degree in mechanical design manufacture and automation and the M.S. degree in mechanical and electronic engineering from Central South University, Changsha, China, in 2003 and 2006, respectively. From 2017, He is currently working toward Ph.D. degree in power electronics and electrical drives at the School of Electrical Engineering and Automation, Harbin Institute of Technology, Harbin, China.

In 2006, he joined the Guangdong Midea Air-Conditioning Equipment CO., LTD, where he has been an Associate Senior Engineer of Light Industrial Refrigeration Equipment Engineering since 2014. His current research interests include advanced control of permanent magnet synchronous motor drives. He has authored more than 13technical papers published in journals and conference proceedings. He is the holder of 46 Chinese patents.

Dawei Ding (M'18) received the B.S and M.S degrees in Electrical Engineering from Hefei University of Technology, in 2014 and 2017, respectively, and the Ph.D degree in Electrical Engineering from Harbin Institute of Technology (HIT), in 2021. Currently, he is an Assistant Professor in School of Electrical Engineering and Automation, HIT. From 2020 to 2021, he was a visiting Ph.D in Technical University of Denmark. He has authored more than 10 journal papers in IEEE Transactions. His current research interests include advanced control of permanent magnet synchronous motor drives and electrolytic capacitorless AC motor drives.

Zekun Ren received the B.S. degree in Electrical Engineering and Automation from Northeast Agricultural University, Harbin, China, in 2020, and the M.S. degree in Electrical Engineering from Harbin Institute of Technology (HIT), Harbin, China, in 2022. Currently, he is working toward the Ph.D. degree in power electronics and electrical drives in the School of Electrical Engineering and Automation, Harbin Institute of Technology. His current research interest includes electrolytic capacitorless motor drives.

Gaolin Wang (M'13, SM'18) received the B.S., M.S. and Ph.D. degrees in Electrical Engineering from Harbin Institute of Technology, Harbin, China, in 2002, 2004 and 2008 respectively.

In 2009, he joined the Department of Electrical Engineering, Harbin Institute of Technology as a Lecturer, where he has been a Full Professor of Electrical Engineering since 2014. From 2009 to 2012, he was a Postdoctoral Fellow in Shanghai Step Electric Corporation, where he was involved in the traction machine control for direct-drive elevators. He has authored more than 60 technical papers published in IEEE Transactions. He is the holder of 30 Chinese patents. His current major research interests include permanent magnet synchronous motor drives, position sensorless control of AC motors, and digital control of power converters.

Dr. Wang serves as a Guest Associate Editor of IEEE Transactions on Industrial Electronics, an Associate Editor of IEEE Transactions on Transportation Electrification, IET Electric Power Applications.

Nannan Zhao (M'19) received the B.S. and M.S. degrees in control science and engineering in 2013 and 2015, and the Ph.D. degree in electrical engineering in 2019, all from Harbin Institute of Technology. Currently he is a Postdoctoral Fellow in the School of Electrical Engineering and Automation, Harbin Institute of Technology. In 2021, he joined the Guangdong Midea Air-Conditioning Equipment CO., LTD as a senior engineer. His current research interests include advanced control of permanent magnet synchronous motor drives and position sensor-less control of ac motors. He is a member of IEEE and currently supported by Postdoctoral Innovative Talent Support Program of China.

Lianghong Zhu received the B.S. degree in Mechanical manufacture technology and equipment from Hefei University of Technology, Hefei, China, in 2001，and the M.S. degree in Measuring and Testing Technologies and Instruments from Huaqiao University, Quanzhou, china, in 2004. He is currently working toward Ph.D. degree at Harbin Institute of Technology, Harbin, China.

In 2005, he joined the R&D center of residential air-conditioning division, Midea Group, engaged in air-conditioning inverter controller design and application development. He has authored 10 technical papers published in journals. He has applied for more than 60 patents, of which 5 invention patents and 20 utility model patents have been authorized. In 2014, he won the second prize of China National Science and Technology Progress Award.

Dianguo Xu (M’97-SM’12-F' 16) received the B.S. degree in Control Engineering from Harbin Engineering University, Harbin, China, in 1982, and the M.S. and Ph.D. degrees in Electrical Engineering from Harbin Institute of Technology (HIT), Harbin, China, in 1984 and 1989, respectively.

In 1984, he joined the Department of Electrical Engineering, HIT as an assistant professor. Since 1994, he has been a professor in the Department of Electrical Engineering, HIT. He was the Dean of School of Electrical Engineering and Automation, HIT from 2000 to 2010. He is now the vice president of HIT. His research interests include renewable energy generation technology, power quality mitigation, sensorless vector controlled motor drives, high performance servo system. He published over 600 technical papers.

Dr. Xu is a fellow member of IEEE, an Associate Editor of the IEEE Transactions on Industrial Electronics and the IEEE Journal of Emerging and Selected Topics in Power Electronics. He serves as Chairman of IEEE Harbin Section.